# Valley splitting in low-density quantum-confined heterostructures studied using tight-binding models

Timothy B. Boykin,[1] Gerhard Klimeck,[2,5] Mark Friesen,[3,4] S. N. Coppersmith,[3] Paul von Allmen,[2] Fabiano Oyafuso,[2] and Seungwon Lee[2]

[1]*Department of Electrical and Computer Engineering, The University of Alabama in Huntsville, Huntsville, Alabama 35899, USA*

[2]*Jet Propulsion Laboratory, California Institute of Technology, 4800 Oak Grove Road, MS 169-315, Pasadena, California 91109, USA*

[3]*Department of Physics, University of Wisconsin, Madison, Wisconsin 53706, USA*

[4]*Department of Material Science and Engineering, University of Wisconsin, Madison, Wisconsin 53706, USA*

[5]*Network for Computational Nanotechnology, School of Electrical and Computer Engineering, Purdue University, West Lafayette, Indiana 47907, USA*

(Received 22 January 2004; revised manuscript received 6 May 2004; published 29 October 2004)

A detailed study of reduced-basis tight-binding models of electrons in semiconducting quantum wells is presented. The focus is on systems with degenerate valleys, such as silicon in silicon germanium heterostructures, in the low-density limit, relevant to proposed quantum computing architectures. Analytic results for the bound states of systems with hard-wall boundaries are presented and used to characterize the valley splitting in silicon quantum wells. The analytic solution in a no-spin-orbit model agrees well with larger tight-binding calculations that do include spin-orbit coupling. Numerical investigations of the valley splitting for finite band offsets are presented that indicate that the hard-wall results are a good guide to the behavior in real quantum wells.

DOI: 10.1103/PhysRevB.70.165325 PACS number(s): 73.21.Fg, 73.61.Cw, 73.63.Hs

## I. INTRODUCTION

The presence of degenerate levels in a quantum system is an essential feature of a potential quantum computing device. Two examples are spin degeneracy, used for spintronics[1] and quantum computing,[2] and layer degeneracy in quantum Hall bilayers, leading to ferromagnetism in a two-dimensional electron gas.[3] Spin is also of interest for semiconductor quantum computing devices. Si/SiGe heterostructures with a goal of achieving long spin coherence times are being pursued actively,[2,4,5] since silicon is expected to have longer spin coherence times than GaAs.[5]

Bulk silicon has sixfold degenerate conduction-band *X*-valleys, while in [001]-strained silicon, the relevant degeneracy is reduced to the two *X*-valleys lying along *z*. Since the valley index is a pseudospin, the valley states can also be exploited for quantum devices, similarly to spin states. Indeed, valley "polarization" has recently been observed,[6] while electronic gate control of valley physics has been known for some time.[7]

While potentially useful for other devices, valley degeneracy is problematic in spin quantum computing, for it is a potential source of decoherence and other difficulties.[8] The extraneous valley degree of freedom must be strictly controlled to prevent leakage of quantum information outside the qubit Hilbert space. Therefore, it is of great interest to understand how to lift the valley degeneracy and maximize the splitting between these two valleys. Practically, this involves creating a valley splitting $\Delta_v$ to lift the degeneracy. The quantum system can then be constrained to its valley ground state by lowering the temperature far below the splitting, as demonstrated in Ref. 6.

Although valley splitting has been studied for many years, it is far less well understood than one might expect. For example, no theory has emerged to explain the strong enhancements observed in high magnetic fields[9] and extending to low fields.[10] Other fascinating experiments also reveal aspects of valley physics that remain unexplained.[11]

One impediment to properly understanding valley splitting has been the lack of a strong microscopic foundation, particularly with respect to quantum wells. In these wells, the valley splitting has been calculated in detail in the two-valley effective-mass approximation, [12] and predicted but not explained in superlattice tight-binding calculations.[13] In addition, the ground state of a symmetric device can be of either even or odd parity, depending on the well width. The alternating parity has been predicted before,[14] but only very recently explained.[15]

In a recent paper,[15] we presented results for a single-particle explanation of valley splitting, valid in the limit of low electron density, which is most relevant for quantum computing applications.[5] Employing both simpler, analytic tight-binding models, and more complete tight-binding calculations,[16,17] we showed rough quantitative agreement between the results using the sophisticated modeling and those obtained using a simple one-dimensional tight-binding model. However, in Ref. 15 the analytic formulas for the valley splitting of the simple model are quoted but not derived, and results for only infinite square wells are presented. Real heterostructures have finite band offsets, so it is of great interest to determine the range of well depths for which infinite square well results are a good guide.

This article presents the mathematical details of the derivation of the valley splitting of the simple tight-binding model of Ref. 15 as well as numerical investigations of the behavior of the valley splitting under conditions of finite quantum confinement. Our calculations of the valley splitting differ from previous work on valley splitting using the two-

 

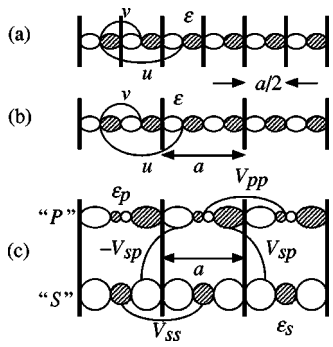


FIG. 1. Sketch of different versions of a simple tight-binding model, all related by basis transformations. White regions are negative, striped regions positive. (a) Single-band model with one *p*-like orbital per atom and one atom per unit cell (length $a/2$). Parameters are $\varepsilon$ (on-site), $v$ (nearest-neighbor), and $u$ (second-nearest-neighbor). (b) Grouping two atoms together in a single cell yields a two-band model with two atoms per unit cell (length $a$), and each atom with one *p*-like orbital. (c) A basis transformation on the middle model using symmetric and antisymmetric combinations yields a two-band model with one atom of two orbitals per unit cell (length $a$). The parameters are: $\varepsilon_s=\varepsilon-v$, $\varepsilon_p=\varepsilon+v$, $V_{ss}=u-v/2$, $V_{pp}=u+v/2$, $V_{sp}=v/2$.

valley effective-mass approximation[12] and using superlattice tight-binding calculations[13] because we have no empirical valley-coupling constant and we solve discrete tight-binding models for quantum wells in real space. Our calculations, furthermore, give an analytic approximation for the valley splitting from a two-band tight-binding model in semiquantitative agreement with multiband tight-binding calculations.

The article is organized as follows. Section II presents the details of the valley splitting calculation for the two-band model along with results, Sec. III discusses the effects of finite-height barriers, and Sec. IV the conclusions. Appendix A discusses the three equivalent descriptions of the simple tight-binding model investigated in the bulk of the paper, while Appendix B discusses the application of the method to more complicated tight-binding models.

## II. VALLEY SPLITTING IN THE TWO-BAND MODEL

### A. Infinite quantum well

In order to obtain an analytic expression we employ the simplest possible model for the conduction band of Si, a two-band model (see Fig. 1). The underlying bulk model is discussed in detail in Appendix A. Since the two atoms in a unit cell are identical, each with a single $p_z$-like orbital, the orbital coefficients may be indexed by atom without ambiguity. (This is equivalent to describing the problem as a one-band model; Appendix A details the requisite basis transformation.) Because the analysis is also somewhat simpler for an odd number of atoms (half-integral number of unit cells), we present this case, later generalizing the results to an even number of atoms.

For a quantum well of $2N+1$ atoms, the wave function in the localized-orbital basis using atom-indexed notation is

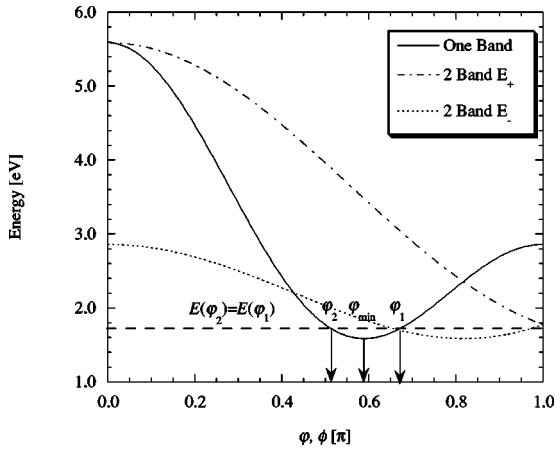


FIG. 2. Bulk dispersions for the one- and two-band models with the same parameters. The one-band phase is $\varphi=k^{(1)}a/2$ and the two-band phase is $\phi=k^{(2)}a$ (the one-band cell is half as long as the two-band cell). The parameters are: $\varepsilon=3.0$ eV, $v=0.682\,640$ eV, $u=0.611\,705$ eV. Also shown are two phases having the same energy as discussed in Sec. II B. For clarity only one energy for the one-band model is shown.

$$|\Psi\rangle = \sum_{n=-(N+2)}^{N+2} C_n |z;n\rangle, \tag{1}$$

where $|z;n\rangle$ denotes the $p_z$-like orbital on the $n$th atom (see Fig. 1). Within the quantum well, the Schrödinger equation, using matrix elements shown in Fig. 1(a), reads

$$uC_{n-2} + vC_{n-1} + [\varepsilon - E]C_n + vC_{n+1} + uC_{n+2} = 0, \tag{2}$$

$$|n| \leqslant N-2,$$

while application of the hard-wall boundary conditions

$$C_{-(N+2)} = C_{-(N+1)} = C_{N+2} = C_{N+1} = 0 \tag{3}$$

results in the following quantum well Hamiltonian matrix of dimension $(2N+1)$:

$$\underline{\mathbf{H}}_{2N+1}(\varepsilon,v,u) = \begin{bmatrix} \varepsilon & v & u & 0 & \cdots & \cdots & 0 \\ v & \varepsilon & v & u & 0 & & \vdots \\ u & v & \varepsilon & v & u & \ddots & \vdots \\ 0 & \ddots & \ddots & \ddots & \ddots & \ddots & 0 \\ \vdots & \ddots & u & v & \varepsilon & v & u \\ \vdots & \ddots & 0 & u & v & \varepsilon & v \\ 0 & \cdots & \cdots & 0 & u & v & \varepsilon \end{bmatrix}. \tag{4}$$

This Hamiltonian can be analyzed analytically because for a flatband quantum well, the wave function for a bound state of energy $E_n$ can only be a superposition of the available propagating and evanescent bulk states at the same energy, $E_n$. The exact details of this superposition are determined by the boundary conditions, in the present study taken to be hard walls. The situation of interest is that encountered in Si $X$-valley conduction-band quantum wells (see Fig. 2) in the energy range in which there are two degenerate pairs of propagating states. The dimension of the generalized

eigenproblem[18] for the bulk material, which is equal to 4, confirms that there are no evanescent states at these energies. Each member of the quartet of Bloch states which serves as the basis for a quantum well state takes the form (up to a normalization)

$$|\psi_{\varphi}^{B}\rangle = \sum_{n=-(N+2)}^{N+2} e^{in\varphi}|z;n\rangle; \quad \varphi = ka/2; \quad -2\pi/a < k \leqslant 2\pi/a, \tag{5}$$

where in the atom-indexed treatment it must be remembered that each atom occupies length $a/2$. Note that two atoms beyond the quantum well on each side must be included: only the total wave function need vanish there, not its separate components. The total wave function is then a superposition of this quartet of Bloch states, given by

$$|\Psi\rangle = \sum_{j=1}^{2} \{b_j^{(+)}|\psi_{\varphi_j}^{B}\rangle + b_j^{(-)}|\psi_{-\varphi_j}^{B}\rangle\}; \quad \varphi_j = k_j a/2. \tag{6}$$

Exploiting the symmetry of the well by combining counterpropagating states into parity eigenstates simplifies matters. Since the well is centered about the zeroth atom, no centering phase enters; comparison of Eqs. (1) and (6) shows that the coefficients $C_n$ are either even ($e$) or odd ($o$) and may be written

$$C_n^{(e)} = a_1^{(e)} \cos(n\varphi_1^{(e)}) + a_2^{(e)} \cos(n\varphi_2^{(e)}), \tag{7}$$

$$C_n^{(o)} = a_1^{(o)} \sin(n\varphi_1^{(o)}) + a_2^{(o)} \sin(n\varphi_2^{(o)}), \tag{8}$$

where in terms of the one-band wave vector, $k_j^{(\alpha)}$, $\varphi_j^{(\alpha)} = k_j^{(\alpha)} a/2, \alpha \in \{e,o\}$.

Imposing the boundary conditions [Eq. (3)] on each of Eqs. (7) and (8) results in a homogeneous system for the coefficients $a_j^{(\alpha)}$, whose determinant must vanish for a nontrivial solution to exist. For even $C_n$ [Eq. (7)], the allowed wave vectors are determined by the simultaneous solution of the secular equation

$$\cos[(N+1)\varphi_1^{(e)}]\cos[(N+2)\varphi_2^{(e)}] - \cos[(N+2)\varphi_1^{(e)}]\cos[(N+1)\varphi_2^{(e)}] = 0 \tag{9}$$

along with the bulk equation

$$E(\varphi_1^{(e)}) = E(\varphi_2^{(e)}), \tag{10}$$

where the bulk energy is given in Appendix A, Eq. (A4). For odd $C_n$ one must solve the pair of equations

$$\sin[(N+1)\varphi_1^{(o)}]\sin[(N+2)\varphi_2^{(o)}] - \sin[(N+2)\varphi_1^{(o)}]\sin[(N+1)\varphi_2^{(o)}] = 0, \tag{11}$$

$$E(\varphi_1^{(o)}) = E(\varphi_2^{(o)}). \tag{12}$$

### B. Approximate expression for the valley splitting

The attraction of the two-band model above is that Eqs. (9)–(12) are sufficiently simple that analytic solution of them is possible. For the problem of valley splitting in Si quantum wells,[15,19,20] approximations for the energies themselves are not so important; instead, approximations for the difference in energy between successive bound states, referred to as the valley splitting, is of greater interest.[4] The two-band model allows for a particularly illuminating and useful approximation for valley splitting.

The first step is to rewrite Eqs. (9) and (11) using trigonometric relations. To simplify the notation, express $N$ in terms of the dimensionless length. For the atom-indexed derivation given above, $S=2N+1$. For an integral number of unit cells (even number of atoms) $S=2N_{cell}$, where $N_{cell}$ is the total number of two-band unit cells in the quantum well. Using trigonometric relations, Eq. (9) is rewritten as

$$\sin(\delta^{(e)})\sin[(S+2)\overline{\varphi}^{(e)}] + \sin(\overline{\varphi}^{(e)})\sin[(S+2)\delta^{(e)}] = 0, \tag{13}$$

while Eq. (11) becomes

$$-\sin(\delta^{(o)})\sin[(S+2)\overline{\varphi}^{(o)}] + \sin(\overline{\varphi}^{(o)})\sin[(S+2)\delta^{(o)}] = 0, \tag{14}$$

where the individual phases are expressed in terms of differences and averages, as

$$\delta^{(\alpha)} = (\varphi_1^{(\alpha)} - \varphi_2^{(\alpha)})/2, \quad \overline{\varphi}^{(\alpha)} = (\varphi_1^{(\alpha)} + \varphi_2^{(\alpha)})/2; \quad \alpha \in \{e,o\}. \tag{15}$$

It is important to note that while the $\overline{\varphi}^{(\alpha)}$ will be close to the valley minimum-phase, $\varphi_{min}$ [calculated with Eq. (A4) of Appendix A], they will not exactly equal it, since the valley will be somewhat asymmetric. Observe that Eqs. (13) and (14) differ only in the sign of the first term. This fact, together with the approximate location of the $X$-valley minimum, leads to a useful approximation for the splitting.

As shown in Fig. 2, for a reasonably symmetric $X$-valley, the phase of the valley minimum ($\varphi_{min}$) will be approximately the average of the two Bloch state phases: $\varphi_{min} \approx \overline{\varphi}^{(\alpha)}$. Using this approximation in Eqs. (13) and (14) leads to two significant conclusions. First, when $(S+2)\varphi_{min} = m\pi$, for $m$ an integer, the splitting should be minimized since in this case the first term of each is approximately zero and Eqs. (13) and (14) are therefore almost identical. Second, when $(S+2)\varphi_{min} = (2m+1)\pi/2$, for $m$ an integer, the splitting should be maximized, since Eqs. (13) and (14) differ the most. Two additional useful observations follow from these: The splitting oscillates with the well width, and the parity of the ground state depends upon the well width, as observed in Refs. 14 and 15. The varying parity can be seen by considering the maximal splitting case, in which the sign of the first term oscillates with the quantum well width.

The key insight leading to the approximate splitting is the realization that the lowest-lying states of any reasonable length quantum well will have phases differing only slightly from that of the valley minimum. Hence, the phases of the two cosines in Eq. (7) and those of the two sines in Eq. (8) will be close. Since sums and differences of cosines and sines may be expressed as products of cosines and sines, one at the average of the two phases, the other at the average of

the difference in the two phases, the two lowest states will have essentially the same, slowly varying, cosine-like envelope, but opposite-parity underlying fast oscillations.

Accordingly, Eqs. (13) and (14) can be rewritten in complex form and subjected to a perturbation treatment[21] to calculate the $\delta^{(\alpha)}$ to any desired order. For the present purpose, however, a lowest-order expansion is all that is required and is most easily carried out by taking advantage of the above physical and mathematical insights. The lowest two bound states of this quantum well should both have cosine-like envelopes characterized by a phase $\delta^{(\alpha)} \approx \pi/S$, which will be small for any reasonable quantum well, so that $\sin(\delta^{(\alpha)}) \approx \delta^{(\alpha)}$. Similarly, the argument of the last sine of Eqs. (13) and (14) may be approximated by first using a trigonometric relation to reduce it:

$$\sin[(S+2)\delta^{(\alpha)}] = -\sin[(S+2)\delta^{(\alpha)} - \pi] \approx \pi - (S+2)\delta^{(\alpha)}. \tag{16}$$

Making these small-angle approximations in Eqs. (13) and (14) yields

$$\delta^{(\alpha)} \approx \frac{\pi}{(S+2) \mp \dfrac{\sin[(S+2)\overline{\varphi}^{(\alpha)}]}{\sin(\overline{\varphi}^{(\alpha)})}} \approx \frac{\pi}{(S+2)} \pm \frac{\pi}{(S+2)^2}\frac{\sin[(S+2)\overline{\varphi}^{(\alpha)}]}{\sin(\overline{\varphi}^{(\alpha)})}, \quad \alpha = \begin{cases} e \\ o \end{cases}, \tag{17}$$

where the upper signs are taken for $\alpha = e$ and the lower signs for $\alpha = o$.

The average phases must now be related back to the valley minimum phase, $\varphi_{min}$; this is easily accomplished by using bulk relation Eq. (A4) and trigonometric relations to find

$$\cos(\varphi_1^{(\alpha)}) + \cos(\varphi_2^{(\alpha)}) = 2\cos(\varphi_{min}) \Rightarrow \cos(\overline{\varphi}^{(\alpha)})\cos(\delta^{(\alpha)}) = \cos(\varphi_{min}). \tag{18}$$

Since the deviation of the average phase from the valley minimum ought to be small—most valleys are not grossly asymmetric, at least for the lowest states—it is convenient to recast Eq. (18) in terms of the separation

$$\Delta^{(\alpha)} = \overline{\varphi}^{(\alpha)} - \varphi_{min} \tag{19}$$

and make small-angle approximations for $\delta^{(\alpha)}$ and $\Delta^{(\alpha)}$ to get a quadratic equation for $\Delta^{(\alpha)}$. The relevant root of this equation [keeping in mind that $\tan(\varphi_{min}) < 0$] to lowest order in $\delta^{(\alpha)}$ is

$$\Delta^{(\alpha)} \approx -\frac{1}{2}\cot(\varphi_{min})[\delta^{(\alpha)}]^2. \tag{20}$$

The valley splitting (energy difference between the states of the lowest bound doublet) may now be calculated. Using Eq. (A4), $\cos(\varphi_{min}) = -v/4u$, and trigonometric relations, the splitting may be expressed as

$$E(\varphi_1^{(o)}) - E(\varphi_1^{(e)}) = 16u\sin\left(\frac{\varphi_1^{(o)} + \varphi_1^{(e)}}{2}\right)\sin\left(\frac{\varphi_1^{(o)} - \varphi_1^{(e)}}{2}\right) \times \left\{\sin\left(\frac{\varphi_1^{(o)} + \varphi_{min}}{2}\right)\sin\left(\frac{\varphi_1^{(o)} - \varphi_{min}}{2}\right) + \sin\left(\frac{\varphi_1^{(e)} + \varphi_{min}}{2}\right)\sin\left(\frac{\varphi_1^{(e)} - \varphi_{min}}{2}\right)\right\}. \tag{21}$$

The term in curly braces in Eq. (21) may be expanded to lowest order in $(S+2)^{-1}$ using Eqs. (17) and (19). Substituting this expansion into Eq. (21) results in

$$E(\varphi_1^{(o)}) - E(\varphi_1^{(e)}) \approx \frac{16\pi u}{(S+2)}\sin(\varphi_{min}) \times \sin\left(\frac{\varphi_1^{(o)} + \varphi_1^{(e)}}{2}\right)\sin\left(\frac{\varphi_1^{(o)} - \varphi_1^{(e)}}{2}\right). \tag{22}$$

Similarly, expansions to lowest order in $(S+2)^{-1}$ give for the remaining two sines in Eq. (22),

$$\sin\left(\frac{\varphi_1^{(o)} + \varphi_1^{(e)}}{2}\right) \approx \sin(\varphi_{min}), \tag{23}$$

$$\sin\left(\frac{\varphi_1^{(o)} - \varphi_1^{(e)}}{2}\right) \approx -\frac{\pi}{(S+2)^2}\frac{\sin[(S+2)\varphi_{min}]}{\sin(\varphi_{min})}, \tag{24}$$

so that the splitting is

$$E(\varphi_1^{(o)}) - E(\varphi_1^{(e)}) \approx -\frac{16\pi^2 u}{(S+2)^3}\sin(\varphi_{min})\sin[(S+2)\varphi_{min}], \tag{25}$$

where Eq. (25) is derived for the atom-indexed model. The magnitude of the splitting is easily recast in terms of the two-band model using Appendix A 1:

$$\Delta E_1 = |E^{(o)} - E^{(e)}| \approx \frac{16\pi^2 u}{(S+2)^3}\sin\left(\frac{\phi_{min}}{2}\right)\left|\sin\left[(S+2)\frac{\phi_{min}}{2}\right]\right|, \tag{26}$$

where, as stated above, $S = 2N_{cell}$, *twice* the number of two-band cells, and the one-band phase $\varphi_{min}$ is related to the two-band phase $\phi_{min}$ via $\varphi_{min} = \pi - \phi_{min}/2$. The notation $\Delta E_1$ emphasizes that the splitting calculated is that between the states of the lowest doublet.

### C. Results

The two-band model is very useful since, lacking valence bands, it can be more readily made to represent the conduction band of Si. The lower two-band dispersion shown in Fig. 2 represents Si as strained to an $Si_{0.8}Ge_{0.2}$ substrate. Figure 3 graphs the magnitude of the splitting of the lowest two confined states versus quantum well length [1 monolayer (ML) = one two-band cell = two atoms] as calculated with the two-band model and NEMO[16] using the $sp^3d^5s^*$ model.[22] The

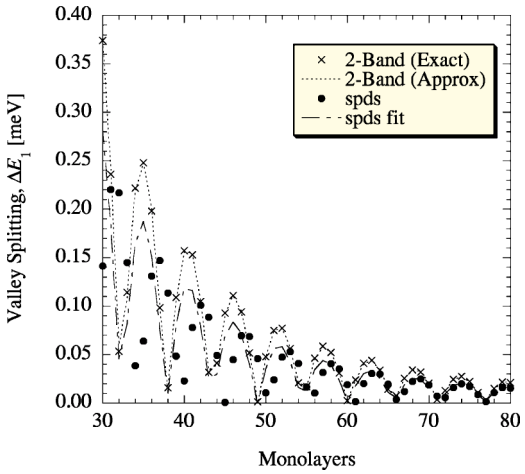


FIG. 3. Valley splitting (magnitude of the energy difference between the states of the lowest doublet) in a strained Si quantum well at zero applied field with hard-wall boundary conditions. Numerical results calculated with NEMO's $sp^3d^5s^*$ model, NEMO *spds*, and the two-band model presented here, two-band (exact), are shown as symbols with no lines. The approximate two-band splitting from Eq. (26), two-band (Approx), along with a fit of the NEMO results to Eq. (26), *spds*-fit, are shown as lines with no symbols, although they are calculated at the same points as the numerical results.

effective mass and minimum of the lower band of the two-band model are chosen to match those of strained bulk Si in the NEMO[16] calculation. Symbols plot calculated points (from direct diagonalization in the two-band model) while lines plot Eq. (26) for the two-band model and an amplitude-scaled version of this equation fit to the NEMO[16] results. Equation (26) is remarkably good for the two-band model for quantum wells over 30 MLs (about 8.1 nm). Most importantly, the simpler and more complete NEMO[16] calculations show the same oscillatory behavior and rate of decay for quantum wells over 30 ML, the two models agree quantitatively for quantum wells over 60 ML (about 16.2 nm).

The most significant feature of Fig. 3 is that both the simpler and more complete tight-binding models predict oscillations in the splitting with well width even without an electric field. This behavior is due to the presence of multiple propagating states in the well, *not* spin-orbit effects, since the two-band model has no spin-orbit coupling, whereas the more complete NEMO[16] $sq^3d^5s^*$ calculation does include spin-orbit.

These oscillations have also been seen by Ohkawa[12] in two-valley effective-mass calculations for silicon quantum wells. However, the commonly employed effective-mass approach requires an empirical valley coupling constant to model valley splitting. This empirical valley coupling constant ultimately depends on the details of the heterostructure, and thanks to the advancement of growth techniques and materials technology, numerous combinations of heterointerfaces are possible in a single device, so that each heterointerface in a device might require its own empirical coupling constant. In contrast, the tight-binding method needs no additional parameters, as the mixture of different propagating states in the well (or valley mixing in the effective-mass framework) is completely determined by the bulk materials models together with the boundary conditions. In addition to quantum wells, the tight-binding method easily models graded junctions, delta-doping confinement, and high electric fields. The tight-binding calculations therefore avoid a significant shortcoming of the effective-mass approach, especially for general purpose heterostructure simulator development.[16,23]

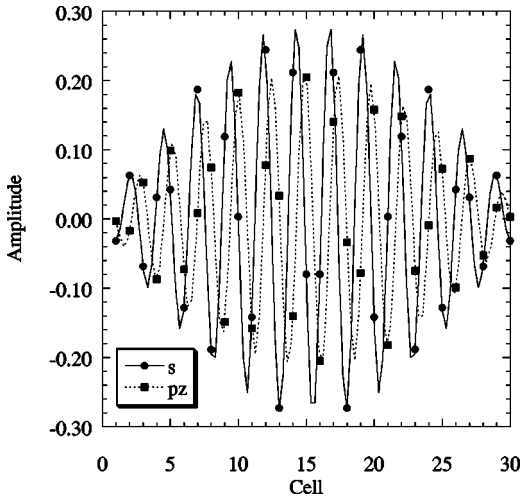


FIG. 4. Ground state *S*- and *Z*-coefficients for a quantum well of 30 cells as calculated in the two-band model.

Figures 4 and 5 plot wave-function results from the two-band model for a 30 ML (i.e., 30 two-band cells or 60 one-band cells) quantum well. Figure 4 graphs the ground state envelopes, Fig. 5 the first excited state envelopes. Symbols are points as calculated by direct diagonalization of the one-band version, transformed to the two-band model using Eqs. (1) and (2). Appendix A 2 gives a detailed discussion of these wave functions.

## III. EFFECTS OF FINITE-HEIGHT BARRIERS

Real heterostructures have finite-height barriers, so it is important to examine the applicability of the foregoing val-

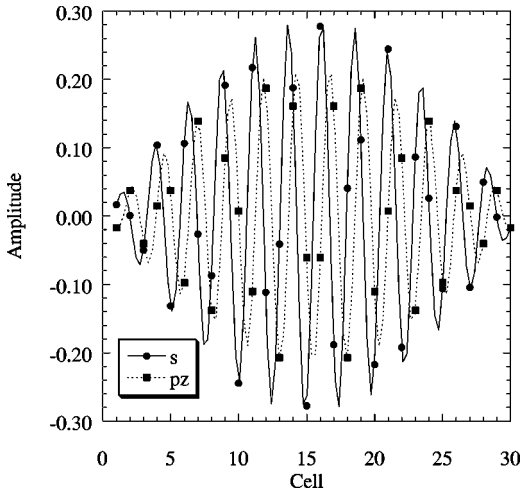


FIG. 5. First excited state *S*- and *Z*-coefficients for a quantum well of 30 cells as calculated in the two-band model.

ley splitting treatment to the practical case. For $Si_{1-x}Ge_x$ barriers the height varies from 0.1 to 0.3 eV for $x=0.2$ and 0.5, respectively.[24] Two approaches are available for modeling the finite barrier problem. The simpler, in terms of both programming and explanation, is to add long barrier regions on either side of the quantum well, and apply hard-wall boundary conditions at the ends of the barriers. Provided that the barriers are sufficiently long, increasing the barrier length will not affect the lowest eigenstates (the ones of interest here). Note that although the Hamiltonian becomes quite large, one must still solve only an ordinary Hermitian eigenvalue problem. The more difficult, but more elegant, approach involves finding the appropriate forward and reverse eigenstates[18] in the barrier regions and expanding the wave function on each side of the well in terms of these states. For a quantum well bound state these decay going into the barriers. This results in a Hamiltonian matrix only slightly larger than that required for the quantum well with hard walls discussed above, but now one must solve a non-Hermitian eigenvalue problem, with the further complication that the expansion states themselves depend on the energy eigenvalues, requiring an iterative solution.

Because it is considerably easier to program and modern desktop PCs are more than adequate in terms of memory and speed for the two-band model, we investigate the effects of finite barriers using the simpler method of adding long confining regions. The case of symmetric barriers is the simplest and incorporates the relevant physics and thus is treated here. We likewise adopt the simplest treatment for finite barriers, shifting the on-site parameter in the barriers up relative to that in the well. The neighbor-coupling parameters $v$ and $u$ could also be changed, affecting the complex bands in the barriers, but the overall physics would be similar. Thus, we opt for the simplest barrier treatment.

The Hamiltonian is partitioned into three regions; each of the barriers is taken to comprise $B$ atoms and the well $W$ atoms. The Hamiltonian is then written

$$\underline{\mathbf{H}} = \begin{bmatrix} \underline{\mathbf{H}}_B(\varepsilon_B,v,u) & \underline{\mathbf{P}} & \underline{\mathbf{0}} \\ \underline{\mathbf{P}}^\dagger & \underline{\mathbf{H}}_W(\varepsilon,v,u) & \underline{\mathbf{P}} \\ \underline{\mathbf{0}} & \underline{\mathbf{P}}^\dagger & \underline{\mathbf{H}}_B(\varepsilon_B,v,u) \end{bmatrix}, \quad (27)$$

$$\underline{\mathbf{P}} = \begin{bmatrix} 0 & \cdots & \cdots & 0 \\ 0 & \ddots & \ddots & \vdots \\ u & \ddots & \ddots & \vdots \\ v & u & 0 & 0 \end{bmatrix},$$

where $\underline{\mathbf{P}}$ is a $B\times W$ matrix, the square matrices $\underline{\mathbf{H}}_B$ and $\underline{\mathbf{H}}_W$ take the form of Eq. (4), and $\varepsilon_B > \varepsilon$. Hard-wall boundaries correspond to the limit $\varepsilon_B \to \infty$. As discussed above, in this case it is not necessary to explicitly include any of the barrier layers. (See also Ref. 25 for a rigorous treatment in the single-band nearest-neighbor tight-binding model.)

The numerical investigations cover well widths of 5–100 cells (10–200 atoms). The dimension of Hamiltonian Eq. (27) is taken to be 400 (i.e., 400 atoms or 200 cells), which was found to be sufficiently large that increasing the matrix size did not change the results. The on-site energy difference $\varepsilon_B - \varepsilon$ was varied between 0 and 10 eV. All calculations were carried out for an integral number of cells (i.e., an even number of atoms) so that the two-band viewpoint applies without ambiguity.

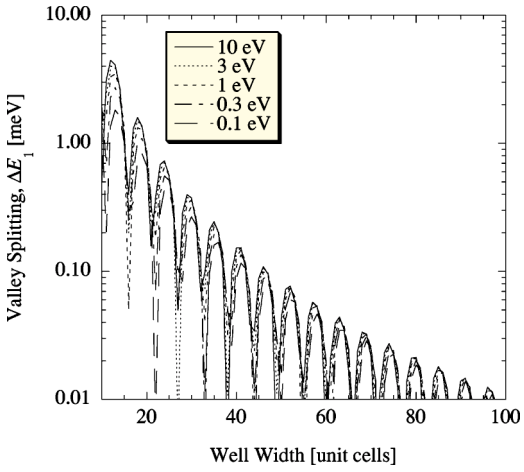


FIG. 6. Valley splitting (magnitude of the energy difference between the states of the lowest doublet) versus well width for quantum wells with band offsets ranging from 0.1 to 10 eV. The behavior is qualitatively similar for the entire range of band offsets, indicating that the hard-wall limit is a good starting point for real quantum wells. For typical experimental well widths, roughly 20 unit cells, the hard-wall limit is a reasonably good estimate of the splitting in wells of depth 0.1 eV or greater.

Figure 6 shows the valley splitting as a function of well width for several different band offsets. (The results for infinite square wells are indistinguishable on the scale of the graph from those for the 10-eV wells.) It is immediately clear that the qualitative behavior of the valley splitting is the same for well depths of order 0.1 eV as for infinite square wells, displaying oscillations as a function of width with the same period (though with a phase that depends slightly on well depth). Figure 7 shows a measure of the fractional change in the valley splitting as a function of well width. The data for this graph were obtained by selecting those points that are local maxima in the splitting-versus-width curve for

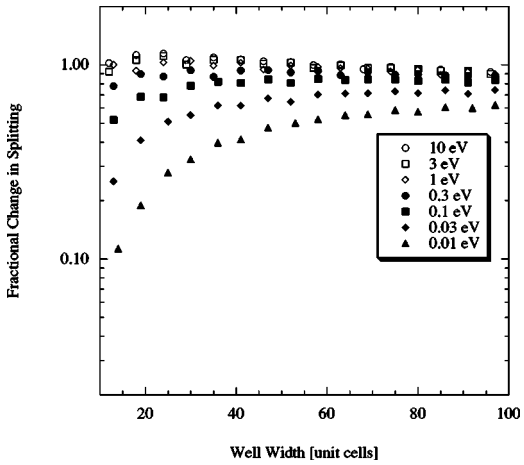


FIG. 7. Fractional change in the valley splitting (see Sec. III) versus well width for well depths ranging from 0.01 to 10 eV.

each well depth, fitting the 10 eV data thus obtained to a power law form, and then dividing the splitting for each well depth and width by the 10 eV fit function. This procedure alleviates the difficulty that comparing valley splittings at two different well depths and the same well widths is complicated by the different phases of the oscillations for different well depths. The figure demonstrates that for typical well widths of 20 unit cells, the valley splitting is of the same order of magnitude as that of the infinite well for well depths down to 0.1 eV.

It is interesting to ask what sets the scale at which the finite-depth corrections to the valley splitting become significant. One candidate scale is the confinement energy, defined as the difference in energy between the ground state of the infinite well and of the finite well. The relation between valley splitting and confinement energy is not simple because the splitting arises from a delicate cancellation, and the leading corrections in powers of inverse well width are identical for the two lowest states. Our numerical results for several different well widths indicate that both the confinement energy and the valley splitting change by roughly 50% when the well depth is decreased from infinity down to 0.1 eV.

## IV. CONCLUSIONS

The conventional technique for finding the bound states of quantum wells modeled using the empirical tight-binding method involves diagonalizing what is often a very large Hamiltonian matrix. This numerical technique differs greatly from that used to solve the infinite square well of elementary quantum mechanics, in which only the bulk eigenstates (plane waves) and $E(k)$ dispersion in the well are necessary. As shown here, a similar approach can be used with tight-binding models when hard-wall (infinite barrier) boundary conditions are enforced.

This approach has the additional virtue of yielding analytic results for smaller (two-band) tight-binding models. Here, the zero-field splitting between the lowest two states in strained silicon quantum wells is computed using this approach. The analytic results highlight the rich interference between multiple propagating states in the well, which is responsible for the alternating parity of the ground state and the oscillations with well width (even at zero electric field) in these structures. In contrast, the conventional, purely numerical approach of diagonalizing a large Hamiltonian matrix provides no insights into these phenomena. Finally, the infinite square well model has been shown to be appropriate for most situations of interest in quantum-computing devices.

## ACKNOWLEDGMENTS

We acknowledge useful conversations with R. Joynt and M. A. Eriksson. Work at JPL, UAH, and UW was sponsored in major proportion by the U. S. Army Research Office through the ARDA program and directly through ARDA. The work at UW was also supported by the National Science Foundation through the MRSEC and QuBIC programs. The work at Purdue was supported by the National Science Foundation, Grant No. EEC-0228390. Part of the work described in this publication was carried out at the Jet Propulsion Laboratory, California Institute of Technology under a contract with the National Aeronautics and Space Administration. Funding was provided at JPL under grants from ARDA, ONR, and JPL.

## APPENDIX A: DETAILS OF THE TWO-BAND MODEL

### 1. Bulk model

The simplest model that can accurately reproduce the lowest conduction band of silicon can be described in one of three ways, completely equivalent insofar as they are related by a change of basis. One basis, producing a two-band model, consists of a unit cell of two identical atoms, each with a single *p*-like orbital, and having second-nearest-neighbor interactions [Fig. 1(b)]. Replacing these orbitals by sums and differences results in an identical two-band model, now with only one atom per unit cell, but two orbitals (*s*- and *p*-like) per atom and only nearest-neighbor interactions [Fig. 1(c)]. The unit cell size is the same as in the two-*p*-orbital two-band model. The third description is of a one-band model, with a single atom unit cell (half the size of the two-band unit cell), each atom having one *p*-like orbital [Fig. 1(a)]. This basis, like the first, has second-near-neighbor interactions.

Each of the three equivalent descriptions plays an important role in solving and interpreting the results of quantum-confined problems. Analytic results are most readily obtained using the one-band model [Fig. 1(a)]. Wave-function plots, however, are much more easily interpreted in terms of the two-band, nearest-neighbor $(S,Z)$ model [Fig. 1(c)]. The two-band, second-nearest-neighbor model [Fig. 1(b)] links the other two; it is particularly easy to translate expressions for the splitting from the one-band model to this two-band model. Although the one-band treatment of a quantum well is the same for either an even or odd number of atoms in the well, rigorous correspondence with the two-band $(S,Z)$ model implies an even number of atoms. Since bulk $E(k)$ relations are needed to find the eigenstates of a flatband quantum well with hard walls, the equivalence of the three descriptions must be established first.

Figure 1 illustrates the transformations linking a two-band (two orbital per atom, one atom per cell [Fig. 1(c)] model to the one-band (one *p*-orbital per atom, one atom per cell [Fig. 1(a)] model. The connection can be seen in the following way. A chain of $2N$ identical atoms, each with a single *p*-like orbital, may be described equivalently as $2N$ single-atom unit cells of size $a/2$, or $N$ two-atom unit cells of size $a$. The first results in a one-band model, the second a two-band model.[26] As illustrated in Figs. 1(a) and 1(b), both of these single-orbital-per-atom models involve second-nearest-neighbor interactions.

The two-band $(S,Z)$ basis results from defining two new orbitals for each cell (note they have identical centers), as

$$|Z;n\rangle = \frac{1}{\sqrt{2}}[|zA;n\rangle + |zC;n\rangle], \tag{A1}$$

$$|S;n\rangle = \frac{1}{\sqrt{2}}[|zA;n\rangle - |zC;n\rangle], \tag{A2}$$

where $n$ is the cell index and "$A$" and "$C$" label the two atoms in a two-atom cell,[27] results in a chain of $N$ one-atom, two-orbitals-per-atom, cells. Note from Fig. 1(c) that the $Z$ and $S$ orbitals of Eqs. (A1) and (A2) are not exactly atomic-like states, but that they do transform as do their atomic counterparts under symmetry operations of the chain, and that the $S$-orbital has the opposite sign of the atomic $s$-orbital. Also observe that the transformations Eqs. (A1) and (A2) convert the second-nearest-neighbor one-orbital-per-atom model to a nearest-neighbor, two-orbital-per-atom model, and that the four parameters of this two-orbital-per-atom model are uniquely determined by the three parameters of the one-orbital-per-atom model.

The bulk dispersion for the one-band model is trivially obtained. Using the Bloch basis (with the orbital type written in lower case to distinguish the one-band kets from the two-band kets)

$$|z;k^{(1)}\rangle = \frac{1}{\sqrt{2N}}\sum_{n=1}^{2N} \exp\left[\frac{ink^{(1)}a}{2}\right]|z;n\rangle \tag{A3}$$

and matrix elements illustrated in Fig. 1, one immediately arrives at the dispersion

$$E(\varphi) = \varepsilon + 2v\,\cos(\varphi) + 2u\,\cos(2\varphi); \quad \varphi = k^{(1)}a/2 \tag{A4}$$

with a Brillouin zone extending over the range $-2\pi/a < k^{(1)} \leqslant 2\pi/a$ (the cell size is $a/2$). The phase which minimizes $E(\varphi)$ is denoted $\varphi_{min}$. It must be remembered that the index $n$ stands for different cells in the one- and two-band descriptions.

For the two-band model, the Bloch sums basis states are

$$|\omega;k^{(2)}\rangle = \frac{1}{\sqrt{N}}\sum_{n=1}^{N} \exp[ink^{(2)}a]|\omega;n\rangle; \quad \omega \in \{S,Z\}, \tag{A5}$$

which in the basis $\{|S;k\rangle, |Z;k\rangle\}$ yields the Hamiltonian matrix

$$\underline{\mathbf{H}}_2 = \begin{bmatrix} \varepsilon_s + 2V_{ss}\,\cos(\phi) & -i2V_{sp}\,\sin(\phi) \\ i2V_{sp}\,\sin(\phi) & \varepsilon_p + 2V_{pp}\,\cos(\phi) \end{bmatrix}; \quad \phi = k^{(2)}a \tag{A6}$$

with a Brillouin zone extending over the range $-\pi/a < k^{(2)} \leqslant \pi/a$. It is essential to keep in mind that the wave vectors $k^{(1)}$ of the one-band and $k^{(2)}$ of the two-band models are different. Expressing the two-band tight-binding parameters in terms of the one-band parameters, and employing trigonometric relations, the eigenvalues of this Hamiltonian matrix are

$$E_{\pm}(\phi) = \varepsilon \pm 2v\,\cos(\phi/2) + 2u\,\cos(\phi). \tag{A7}$$

Figure 2 displays bulk dispersions for both models using parameters appropriate for strained Si in SiGe modulation-doped heterostructures,[15] $\varepsilon = 3.0$ eV, $v = 0.682\,640$ eV, $u = 0.611705$ eV; each model has an indirect minimum like that of Si. Figure 2 shows that the two models are equivalent, being related by zone folding. Setting $\varphi = \phi/2, \varphi: 0 \rightarrow \pi/2$ in Eq. (A4) yields the $E_+$ band of Eq. (A7), while setting $\varphi = \pi - \phi/2, \varphi: \pi/2 \rightarrow \pi$ in Eq. (A4) yields the $E_-$ band of Eq. (A7).

### 2. Wave functions in an infinite quantum well

Figures 4 and 5 plot wave-function results from the two/one-band model for a 30 ML (i.e, 30 two-band cells or 60 one-band cells) quantum well. Figure 4 graphs the ground state envelopes and Fig. 5 the first excited state envelopes. Symbols are points as calculated by direct diagonalization of the one-band version, transformed to the two-band model using Eqs. (A1) and (A2). These wave-function plots are most remarkable, for they in no way resemble what one expects for the ground state and first excited state of a quantum well. While there is a cosine-like envelope, there are also underlying fast oscillations, and, most strikingly of all, *both* of the lowest two states share this envelope.

These results are fully explained by the foregoing analysis. Consistent with a well located in layers 1–30, the wave-function center is 15.5 (the two-band coefficients must vanish at layers 0 and 31). For the lower state, the $S$-coefficients are sums of cosines and the $Z$-coefficients are sums of sines, at phases $\phi_2^{(e)} = 0.8515\pi$, $\phi_1^{(e)} = 0.7880\pi$, corresponding to bulk states just above the valley minimum located at $\phi_{min} = 0.82\pi$ (see $E_-$ in Fig. 2). For the first excited state the $S$-coefficients are sines and the $Z$-coefficients cosines, with phases $\phi_2^{(o)} = 0.8525\pi$, $\phi_1^{(o)} = 0.7870\pi$. The addition of two sines or cosines of nearly equal argument explains the slow cosine-like envelope and fast oscillations underneath. This *envelope* is just what one might expect for the ground state of a direct-gap quantum well of 30 sites (31 intervals), $\pi/31 \approx 0.0323\pi$, since the offsets of the states versus the minimum, $\phi_2^{(e)} - \phi_{min} \approx 0.0315\pi$, $\phi_{min} - \phi_1^{(e)} \approx 0.0320\pi$, $\phi_2^{(o)} - \phi_{min} \approx 0.0325\pi$, and $\phi_{min} - \phi_1^{(o)} \approx 0.0330\pi$, are nicely clustered about this central value. The next two states (second and third excited, not shown) are likewise paired, having a common sine-like envelope characterized by $\delta^{(e)} \approx \delta^{(o)} \approx 2\pi/31$. Finally, results for a well of 31 two-band cells (not shown) demonstrate the expected changing parity of the ground state, for in this case the lower state is odd ($S$-coefficients are sines and $Z$-coefficients are cosines). Without the analysis, only numerical results would be available, and these wave functions would have been difficult to explain and interpret.

## APPENDIX B: EXTENSION TO A FOUR-BAND MODEL

The four-band model represents an intermediate between the simple two-band model and more complete, multiband tight-binding models: Alhough far from perfect,[28] it is the simplest model with a two-atom, multiple-orbital-per-atom basis. Consequently, the procedures for constructing its quantum-confined wave functions are essentially the same as those for much larger models. Specifically, the procedures for determining the centers of the expansion coefficients and

boundary conditions are readily generalizable to larger models sharing the same geometry, differing only in the larger number of orbitals. Thus, unlike the case with the two-band model, the four-band results can serve as guides for constructing the form and interpreting results of large, multiband calculations, which to date have been restricted to purely numerical results.[13,14]

#### 1. Bulk model

The four-band model is readily extracted from the nearest-neighbor, no-spin-orbit $sp^3$ model by taking advantage of the fact that for in-plane wave vector $\mathbf{k}_{\|}=k_x\mathbf{e}_x+k_y\mathbf{e}_y=\mathbf{0}$, the $s$- and $p_z$-like orbitals are decoupled from $p_x$- and $p_y$-like orbitals in both the Bloch and planar-orbital Hamiltonians. The resulting subspace of $s$- and $p_z$-like orbitals yields a Hamiltonian matrix equivalent to that of a chain of two-atom unit cells, with one $s$- and one $p_z$-like orbital per atom; for an elemental semiconductor such as Si the atoms are, of course, identical.[27] The bulk dispersions for the chain (i.e., under cyclic boundary conditions) are found by diagonalizing the Hamiltonian in the $\{|sA;k\rangle,|zA;k\rangle,|sC;k\rangle,|zC;k\rangle\}$ basis ($A$ and $C$ designate the two atoms in a unit cell):

$$\underline{\mathbf{H}}_4=\begin{bmatrix} \varepsilon_s & 0 & 2v_{ss}\cos(\varphi) & i2v_{sp}\sin(\varphi) \\ 0 & \varepsilon_p & -i2v_{sp}\sin(\varphi) & 2v_{pp}\cos(\varphi) \\ 2v_{ss}\cos(\varphi) & i2v_{sp}\sin(\varphi) & \varepsilon_s & 0 \\ -i2v_{sp}\sin(\varphi) & 2v_{pp}\cos(\varphi) & 0 & \varepsilon_p \end{bmatrix}, \tag{B1}$$

where $\varphi=ka/2$and the tight-binding parameters are illustrated in Fig. 8. The Bloch sum basis states are ($\omega\in\{s,z\}$)

$$|\omega A;k\rangle=\frac{1}{\sqrt{N}}\sum_{n=1}^{N}e^{ikan}|\omega A;n\rangle, \tag{B2}$$

$$|\omega C;k\rangle=\frac{1}{\sqrt{N}}\sum_{n=1}^{N}e^{ika(n+1/2)}|\omega C;n\rangle, \tag{B3}$$

where $n$ indexes the unit cells. Note that the $C$ atom in a cell is taken to lie a distance $a/2$ (one-half unit cell) ahead of the $A$ atom, as shown in Fig. 8.

The four-band Hamiltonian for elemental semiconductors [Eq. (B1)] is further simplified by introducing the change of basis, as

$$|s\pm;k\rangle=\frac{1}{\sqrt{2}}[|sA;k\rangle\pm|sC;k\rangle], \tag{B4}$$

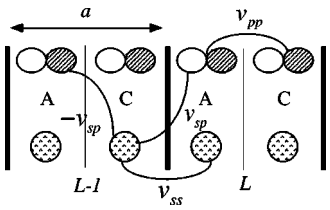


FIG. 8. Unit cells of the four-band model showing on-site and nearest-neighbor parameters.

$$|z\pm;k\rangle=\frac{1}{\sqrt{2}}[|zA;k\rangle\pm|zC;k\rangle], \tag{B5}$$

which block-diagonalizes $\underline{\mathbf{H}}_4$ into two 2-dimensional blocks, as

$$\underline{\mathbf{H}}_2^{(\pm)}=\begin{bmatrix} \varepsilon_s\pm 2v_{ss}\cos(\varphi) & \pm i2v_{sp}\sin(\varphi) \\ \mp i2v_{sp}\sin(\varphi) & \varepsilon_p\pm 2v_{pp}\cos(\varphi) \end{bmatrix}. \tag{B6}$$

The eigenvalues of the matrices Eq. (B6) are readily found; for $\underline{\mathbf{H}}_2^{(+)}$ they are

$$E_{\pm}^{(+)}=\frac{1}{2}\{\varepsilon_s^{(+)}+\varepsilon_p^{(+)}\pm\sqrt{[\varepsilon_s^{(+)}-\varepsilon_p^{(+)}]^2+16v_{sp}^2\sin^2(\varphi)}\}, \tag{B7}$$

while for $\underline{\mathbf{H}}_2^{(-)}$ they are

$$E_{\pm}^{(-)}=\frac{1}{2}\{\varepsilon_s^{(-)}+\varepsilon_p^{(-)}\pm\sqrt{[\varepsilon_s^{(-)}-\varepsilon_p^{(-)}]^2+16v_{sp}^2\sin^2(\varphi)}\}, \tag{B8}$$

where $\varepsilon_\omega^{(\pm)}=\varepsilon_\omega\pm 2v_{\omega\omega}\cos(\varphi),\omega\in\{s,p\}$. (Chadi and Cohen[29] give a treatment of the full $sp^3$ model, including dispersions for other bands and expressions for the energies at various symmetry points.) As an example, an indirect minimum similar to the Si conduction band occurs in the $E_+^{(+)}$ band for $\varepsilon_s=3.0$ eV, $\varepsilon_p=-1.0$ eV, $v_{ss}=-2.0$ eV, $v_{pp}=1.5$ eV, and $v_{sp}=0.25$ eV (not shown). In other respects, however, the bands do not well mimic those of Si.

#### 2. Infinite quantum well

As with the simpler model of Sec. II, setting up the Hamiltonian for the quantum-confined case is actually not

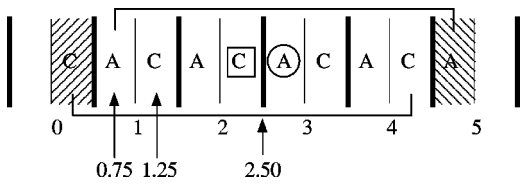


FIG. 9. Computation of anion and cation centers in the four-band model for a quantum well of four unit cells.

necessary since the four-band model provides analytic $E(k)$ relations. (The Hamiltonian is block-tridiagonal with $2\times 2$ blocks.) Just as before, due to the confinement, the wave vector $k$ is not a conserved quantity, and the optimum basis to use is the localized-orbital basis. (In a three-dimensional model this corresponds to the planar-orbital basis with $\mathbf{k}_{\|}=\mathbf{0}$.) In the case of confinement by hard walls, the wave function is completely restricted to the well. In general, the well can contain an integral or half-integral number of unit cells, beginning or ending on $A$ or $C$ atoms and the method works in any of these cases. The method is, however, best illustrated via a concrete example, and here the well is taken to encompass unit cells numbered $1,2,\ldots,N_W$. The wave function is therefore written as

$$|\Psi\rangle = \sum_{j'=0}^{N_W+1} \sum_{\alpha\in\{s,z\}} \sum_{\tau\in\{A,C\}} C_{\alpha\tau;j'}|\alpha\tau;j'\rangle. \tag{B9}$$

The hard-wall boundary is imposed by noting that the wave function must vanish at the $C$ atom just to the left of the well, as

$$C_{sC;0} = C_{zC;0} = 0 \tag{B10}$$

and on the $A$ atom just to the right of the well, as

$$C_{sA;N_W+1} = C_{zA;N_W+1} = 0, \tag{B11}$$

since the well contains an integral number of cells. Note in particular that *no* demand may be made on the coefficients of the $A$ atom in cell 0 or the $C$ atom in cell $N_W+1$, as these coefficients do not exist.

As before, in silicon the interest is in states within the $X$-valleys (corresponding to the $E_+^{(+)}$ band), where there are two pairs of Bloch or propagating states (and no evanescent ones in this model) at a given energy. The quantum well bound states are therefore superpositions of this quartet. The Bloch states are easily found by diagonalizing $\underline{\mathbf{H}}_2^{(+)}$ [Eq. (B6)], and selecting the eigenvector associated with $E_+^{(+)}(\varphi)$. Up to a normalization, each of the Bloch states takes the form

$$|\psi_{2\varphi}\rangle = |sA;k\rangle + |sC;k\rangle + i\rho(\varphi)|zA;k\rangle + i\rho(\varphi)|zC;k\rangle, \tag{B12}$$

where

$$\rho(\varphi) = \frac{\varepsilon_s + 2v_{ss}\cos(\varphi) - E_+^{(+)}(\varphi)}{2v_{sp}\sin(\varphi)}. \tag{B13}$$

Note that $\rho(-\varphi)=-\rho(\varphi)$ and as a result, the state of wave vector $-k$ is related to that of wave vector $+k$ by complex conjugation (there is no spin-orbit interaction in this model).

Equations (B12) and (B13) thus show the form taken by the quartet of Bloch states in the well, which serves as the basis for the total wave function. In the localized-orbital basis, the un-normalized basis states are

$$|\psi_\phi^{QW}\rangle = \sum_{n=1}^{N_W+1} e^{i\phi n}\left[|sA;n\rangle + i\rho\left(\frac{\phi}{2}\right)|zA;n\rangle\right] + \sum_{n=0}^{N_W} e^{i\phi(n+1/2)} \times\left[|sC;n\rangle + i\rho\left(\frac{\phi}{2}\right)|zC;n\rangle\right], \tag{B14}$$

where $\phi=2\varphi=ka$. Note that the $C$ atom in cell 0 and the $A$ atom in cell $(N_W+1)$must be included in the sums as only the *total* wave function (and not its components separately) is required to vanish at these atoms.

Since the well is symmetric, the quantum well eigenstates can be chosen as simultaneous parity eigenstates (with respect to the center of the well). Note, however, that the offset between the $A$ and $C$ atoms means that their coefficients will have different centers. This is illustrated in Fig. 9 for a well composed of four unit cells. In the more general case of a well having an integral number of cells as discussed above, the states (B14) are centered by extracting a phase $\exp(i\theta_0)$, $\theta_0=\phi(N_W/2+3/4)$, since the initial $A$ (in cell 1) has position $3a/4$ and the well length is $N_W a$. Up to normalizations, centered even states are $[\exp(-i\theta_0)|\psi_\phi^{QW}\rangle + \exp(i\theta_0)|\psi_{-\phi}^{QW}\rangle]$ while odd states are $[\exp(-i\theta_0)|\psi_\phi^{QW}\rangle - \exp(i\theta_0)|\psi_{-\phi}^{QW}\rangle]$. Thus, un-normalized even and odd quantum well basis states resulting from a single pair of bulk Bloch states are, in the localized-orbital basis,

$$\begin{aligned}|\psi_\phi^{(e)}\rangle = \sum_{n=1}^{N_W+1}&\left\{\cos\left[\phi\left(n-\frac{N_W}{2}-\frac{3}{4}\right)\right]|sA;n\rangle\right.\\ &\left.-\rho\left(\frac{\phi}{2}\right)\sin\left[\phi\left(n-\frac{N_W}{2}-\frac{3}{4}\right)\right]|zA;n\rangle\right\}\\ +\sum_{n=0}^{N_W}&\left\{\cos\left[\phi\left(n-\frac{N_W}{2}-\frac{1}{4}\right)\right]|sC;n\rangle\right.\\ &\left.-\rho\left(\frac{\phi}{2}\right)\sin\left[\phi\left(n-\frac{N_W}{2}-\frac{1}{4}\right)\right]|zC;n\rangle\right\},\end{aligned} \tag{B15}$$

$$\begin{aligned}|\psi_\phi^{(o)}\rangle = \sum_{n=1}^{N_W+1}&\left\{\sin\left[\phi\left(n-\frac{N_W}{2}-\frac{3}{4}\right)\right]|sA;n\rangle\right.\\ &\left.+\rho\left(\frac{\phi}{2}\right)\cos\left[\phi\left(n-\frac{N_W}{2}-\frac{3}{4}\right)\right]|zA;n\rangle\right\}\\ +\sum_{n=0}^{N_W}&\left\{\sin\left[\phi\left(n-\frac{N_W}{2}-\frac{1}{4}\right)\right]|sC;n\rangle\right.\\ &\left.+\rho\left(\frac{\phi}{2}\right)\cos\left[\phi\left(n-\frac{N_W}{2}-\frac{1}{4}\right)\right]|zC;n\rangle\right\}\end{aligned} \tag{B16}$$

These states are used to construct the even and odd quantum well bound states, from which the quantization conditions result.

Each bound state of an $X$-valley quantum well in the four-band model is a superposition of Bloch states of two different wave vectors; call the associated pair of phases $\phi_1^{(e)}, \phi_2^{(e)}$ for even states and $\phi_1^{(o)}, \phi_2^{(o)}$ for odd states. A general even quantum well bound state is therefore a superposition

$$|\Psi^{(e)}\rangle = a_1^{(e)}|\psi_{\phi_1}^{(e)}\rangle + a_2^{(e)}|\psi_{\phi_2}^{(e)}\rangle, \tag{B17}$$

$$|\Psi^{(o)}\rangle = a_1^{(o)}|\psi_{\phi_1}^{(o)}\rangle + a_2^{(o)}|\psi_{\phi_2}^{(o)}\rangle, \tag{B18}$$

where the $|\psi_{\phi_j}^{(\alpha)}\rangle$ are given in Eq. (B15) for even states and Eq. (B16) for odd states. To enhance readability the superscripts on the phases are suppressed in Eqs. (B17) and (B18); in Eq. (B17) the $\phi_j$ stand for $\phi_1^{(e)}, \phi_2^{(e)}$, while in Eq. (B18) they stand for $\phi_1^{(o)}, \phi_2^{(o)}$. The quantization conditions follow on substituting Eq. (B15) into Eq. (B17) and Eq. (B16) into Eq. (B18) and requiring the total wave function to vanish on the $C$ atom in cell 0 and the $A$ atom in cell $(N_W+1)$. Since symmetry has already been imposed the two requirements yield the same homogeneous system for the coefficients $a_j^{(\alpha)}$.

As with the two-band model above, the bound states are found by requiring the determinant of the appropriate homogeneous system to vanish, while simultaneously satisfying the bulk equation $E_+^{(+)}(\phi_1^{(\alpha)}/2) = E_+^{(+)}(\phi_2^{(\alpha)}/2)$. Thus the even states are found by solving the pair of transcendental equations

$$\rho\left(\frac{\phi_2^{(e)}}{2}\right)\sin\left[\phi_2^{(e)}\left(\frac{N_W}{2}+\frac{1}{4}\right)\right]\cos\left[\phi_1^{(e)}\left(\frac{N_W}{2}+\frac{1}{4}\right)\right] - \rho\left(\frac{\phi_1^{(e)}}{2}\right)\sin\left[\phi_1^{(e)}\left(\frac{N_W}{2}+\frac{1}{4}\right)\right]\cos\left[\phi_2^{(e)}\left(\frac{N_W}{2}+\frac{1}{4}\right)\right] = 0, \tag{B19}$$

$$E_+^{(+)}\left(\frac{\phi_1^{(e)}}{2}\right) = E_+^{(+)}\left(\frac{\phi_2^{(e)}}{2}\right). \tag{B20}$$

Likewise, the odd states are found by solving the pair of transcendental equations

$$\rho\left(\frac{\phi_2^{(o)}}{2}\right)\cos\left[\phi_2^{(o)}\left(\frac{N_W}{2}+\frac{1}{4}\right)\right]\sin\left[\phi_1^{(o)}\left(\frac{N_W}{2}+\frac{1}{4}\right)\right] - \rho\left(\frac{\phi_1^{(o)}}{2}\right)\cos\left[\phi_1^{(o)}\left(\frac{N_W}{2}+\frac{1}{4}\right)\right]\sin\left[\phi_2^{(o)}\left(\frac{N_W}{2}+\frac{1}{4}\right)\right] = 0, \tag{B21}$$

$$E_+^{(+)}\left(\frac{\phi_1^{(o)}}{2}\right) = E_+^{(+)}\left(\frac{\phi_2^{(o)}}{2}\right) \tag{B22}$$

Observe that as with the two-band model above, the effort in determining the bound states is completely independent of the quantum well length. Also note that while these equations yield only semi-analytic information (since a solution of nontrivial transcendental equations is required), this can be useful in and of itself. It is also true that when only the lowest few bound states are needed the simultaneous solution of these equations is easier to program than is the initialization and diagonalization of a large Hamiltonian matrix. More importantly, the wave-function construction procedures developed above are directly applicable to more complete tight-binding models having the same geometry.


[1] S. A. Wolf, D. D. Awschalom, R. A. Buhrman, J. M. Daughton, S. von Molnar, M. L. Roukes, A. Y. Chtchelkanova, and D. M. Treger, Science **294**, 1488 (2001).

[2] B. Kane, Nature (London) **393**, 133 (1998); D. Loss and D. P. DiVicenzo, Phys. Rev. A **57**, 120 (1998); R. Vrijen, E. Yablonovitch, K. Wang, H. W. Jiang, A. Balandin,V. Roychowdhury, T. Mor, and D. DiVincenzo, *ibid.* **62**, 012306 (2000).

[3] K. Yang, K. Moon, L. Zheng, A. H. MacDonald, S. M. Girvin, D. Yoshioka, and S.-C. Zhang, Phys. Rev. Lett. **72**, 732 (1994); K. Moon, H. Mori, Kun Yang, S. M. Girvin, and A. H. MacDonald, Phys. Rev. B **51**, 5138 (1995); L. Brey, H. A. Fertig, R. Côté, A. H. MacDonald, *ibid.* **54**, 16888 (1996).

[4] M. Friesen, P. Rugheimer, D. E. Savage, M. G. Lagally, D. W. van der Weide, R. Joynt, and M. A. Eriksson, Phys. Rev. B **67**, 121301 (2003).

[5] A. M. Tyryshkin, S. A. Lyon, A. V. Astashkin, and A. M. Raitsimring, cond-mat/0303006 (unpublished).

[6] T. Ouisse, D. K. Maude, S. Horiguchi, Y. Ono, Y. Takahashi, K. Murase, and S. Cristoloreanu, Physica B **249–251**, 731 (1998).

[7] R. J. Nicholas, K. von Klitzing, and T. Englert, Solid State Commun. **34**, 51 (1980).

[8] B. Koiller, X. D. Hu, and S. Das Sarma, Phys. Rev. Lett. **88**, 027903 (2002).

[9] Y. P. Shkolnikov, E. P. De Poortere, E. Tutuc, and M. Shayegan, Phys. Rev. Lett. **89**, 226805 (2002); V. S. Khrapai, A. A. Shashkin, and V. T. Dolgopolov, Phys. Rev. B **67**, 113305 (2003).

[10] V. M. Pudalov, A. Punnoose, G. Brunthaler, A. Prinz, and G. Bauer, cond-mat/0104347 (unpublished).

[11] U. Zeitler, H. W. Schumacher, A. G. M. Jansen, and R. J. Haug, Phys. Rev. Lett. **86**, 866 (2001).

[12] F. J. Ohkawa, Solid State Commun. **26**, 69 (1978).

[13] R. D. Graft, D. J. Lohrmann, G. P. Parravicini, and L. Resca, Phys. Rev. B **36**, 4782 (1987).

[14] J.-C. Chiang, Jpn. J. Appl. Phys., Part 1 **33**, 294 (1994).

[15] T. B. Boykin, G. Klimeck, M. A. Eriksson, M. Friesen, S. N. Coppersmith, P. von Allmen, F. Oyafuso, and S. Lee, Appl. Phys. Lett. **84**, 115 (2004).

[16] G. Klimeck *et al.*, in *Proceedings of IEEE DRC, Fort Collins, Colorado, 23–25 June, 1997* (IEEE, Piscataway, NJ, 1997), p. 92; R. C. Bowen *et al.*, J. Appl. Phys. **81**, 3207 (1997); R. Lake,

G. Klimeck, R. C. Bowen, and D. Jovanovic, *ibid.* **81**, 7845 (1997); further NEMO details at http://hpc.jpl.nasa.gov/PEP/gekco/nemo

[17] For recent reviews of the tight-binding method as applied to nanostructures, see: A. DiCarlo, Semicond. Sci. Technol. **18**, R1 (2003); A. Pecchia and A. DiCarlo, Rep. Prog. Phys. **67**, 1497 (2004).

[18] T. B. Boykin, Phys. Rev. B **54**, 7670 (1996); *ibid.* **54**, 8107 (1996).

[19] See, for example: A. B. Fowler, F. F. Fang, W. E. Howard, and P. J. Stiles, Phys. Rev. Lett. **16**, 901 (1966); F. F. Fang and P. J. Stiles, Phys. Rev. **174**, 823 (1968); H. Koehler, M. Roos, and G. Landwehr, Semicond. Sci. Technol. **27**, 955 (1978); R. J. Nicholas, K. von Klitzing, and T. Englert, *ibid.* **34**, 51 (1980); J. Wakabayashi, S. Kimura, Y. Koike and S. Kawaji, Surf. Sci. **170**, 359 (1986); V. M. Pudalov, A. Punnoose, G. Brunthaler, A. Prinz, and G. Bauer, cond-mat/0104347 (unpublished); R. B. Dunford, R. Newbury, F. F. Fang, R. G. Clark, R. P. Starrett, J. O. Chu, K. E. Ismail, and B. S. Meyerson, Solid State Commun. **96**, 57 (1995); S. J. Koester, K. Ismail, and J. O. Cho, Semicond. Sci. Technol. **12**, 348 (1996); P. Weitz, R. J. Haug, K. von Klitzing, and F. Schäffler, Surf. Sci. **361/362**, 542 (1996); D. Monroe, Y. H. Xie, E. A. Fitzgerald, and P. J. Silverman, Phys. Rev. B **46**, 7935 (1992); S. F. Nelson, K. Ismail, J. J. Nocera, F. F. Fang, E. E. Mendez, J. O. Chu, and B. S. Meyerson, Appl. Phys. Lett. **61**, 64 (1992); G. Stöger, G. Brunthaler, G. Bauer, K. Ismail, B. S. Meyerson, J. Lutz, and F. Kuchar, Phys. Rev. B **49**, 10417 (1994).

[20] T. Ando, A. B. Fowler, and F. Stern, Rev. Mod. Phys. **54**, 437 (1982).

[21] E. J. Hinch, *Perturbation methods* (Cambridge University Press, Cambridge, 1991).

[22] J.-M. Jancu, R. Scholz, F. Beltram, and F. Bassani, Phys. Rev. B **57**, 6493 (1998).

[23] G. Klimeck, F. Oyafuso, T. B. Boykin, R. C. Bowen, and P. von Allmen, Comp. Mod. in Eng. Sci. **3**, 601 (2002).

[24] F. Schaffler, Semicond. Sci. Technol. **12**, 1515 (1997).

[25] T. B. Boykin and G. Klimeck, Eur. J. Phys. **25**, 503 (2004).

[26] For a bulk material note that the number of states is the same in either case, but that the Brillouin zone is half as large for the two-band model as for the one-band model.

[27] The labels *A* and *C* for the two (here identical) atoms in a cell are reminiscent of polar semiconductors (e.g., III-V), with which this model can be used.

[28] W. A. Harrison, *Elementary electronic structure* (World Scientific, Singapore, 1999). As Harrison notes, the no-spin-orbit $sp^3$ model from which it is derived is incapable of faithfully reproducing the bandstructure of silicon. This is because in optimizing the conduction band, the valence bands become very inaccurate. (This is not a problem in the two-band model, for it only reproduces the two lowest *conduction* bands.) To a lesser but still significant extent, even the nearest-neighbor, spin-orbit $sp^3s^*$ model shares this shortcoming. See: G. Klimeck, R. C. Bowen, T. B. Boykin, C. Salazar-Lazaro, T. A. Cwik, and A. Stoica, Superlattices Microstruct. **27**, 77 (2000); G. Klimeck, R. C. Bowen, T. B. Boykin, and T. A. Cwik, *ibid.* **27**, 519 (2000).

[29] D. J. Chadi and M. L. Cohen, Phys. Status Solidi B **68**, 405 (1975).